Rotor Ground Capacitance Coupled Harmonic Fault Detection Boundary in Large Synchronous Generators

Yongbin Du*, Wenhao Chao, Qian Zhang, Bingbing Zhao
School of Electrical and Control Engineering, Heilongjiang University of Science and Technology, 2468 University Rd, 150022 Harbin, China
duyongbin@usth.edu.cn; chaowenhao@usth.edu.cn; zhangqian37@usth.edu.cn; zhaobingbing@usth.edu.cn

***Abstract*—Focusing on the impact of rotor-to-ground capacitance on passive ground fault detection in large-scale synchronous generators, this paper proposes an error analysis method using an amplitude deviation factor. Based on the classical equivalent circuit model of the excitation system, the proposed method explicitly incorporates the rotor-to-ground capacitance parameters. It systematically reveals the non-linear mechanism by which ground capacitance affects the harmonic voltage amplitudes of faults on both the DC and the AC sides. This study addresses the limitations of existing research, which is primarily confined to small and medium capacity machines and often neglects the ground capacitance. Verified by computer simulations and field data from large-scale units, the results demonstrate that the proposed method effectively clarifies the detection boundaries and improves fault detection accuracy in high-capacitance scenarios.**

***Index Terms*—Large synchronous generators; Rotor ground fault; Rotor-to-ground capacitance; Amplitude deviation factor; Fault detection accuracy.**

I. INTRODUCTION

Rotor ground faults are recognized as a leading cause of forced outages in synchronous generators [1], [2] influenced by insulation aging, leakage of cooling media, or internal rotor stresses; the insulation-to-ground level degrades, leading to ground faults. Although a single-point ground fault typically does not pose an immediate hazard, it establishes a precarious precondition; the occurrence of a subsequent second-point fault can induce severe mechanical vibrations and thermal damage, inflicting catastrophic destruction on the generator [3]. According to the IEEE standards [4], ground faults account for 18 % to 25 % of forced outages of global thermal power units. However, only 46.3 % of these units are equipped with real-time grounding monitoring, significantly hindering early fault localization.

To address this issue, various protection technologies have been developed, ranging from passive harmonic analysis to injection-based methods. A detailed review of these existing methodologies is presented in Section II. Despite significant progress, the design and implementation of high-sensitivity protection still face numerous challenges.

Liu [5] revealed the inherent difficulties associated with high-resistance ground faults, particularly those within the 5 kΩ to 10 kΩ [4]. The authors in [6]–[8] indicated that protection devices often malfunction due to excitation voltage harmonics during steady-state operation and transient currents flowing through the rotor insulation system. A critical yet frequently overlooked factor is the rotor-to-ground capacitance (C_g) [9]. In large-scale units, typically with capacities of hundreds of megawatts, C_g is non-negligible. With capacitance values commonly ranging from 0.1 μF to 3 μF due to complex cooling structures, the sensitivity of traditional harmonic criteria is severely attenuated. Therefore, this paper establishes a comprehensive error analysis framework. Based on an equivalent model explicitly incorporating capacitance parameters, this study seeks to quantify the influence mechanism of rotor capacitance on detection sensitivity and rigorously define the fault detection boundaries for large-scale synchronous generators under strong capacitance effects.

II. RELATED WORKS

The detection of ground faults on the rotor is critical for the safety of large-scale synchronous generators. With the increasing capacity of generator units towards the gigawatt class, the characteristics of ground faults have evolved, presenting significant challenges to traditional protection schemes.

Recent field investigations have revealed that rotor ground faults in large-scale units are rarely simple metallic short circuits; instead, they often exhibit complex non-linear behaviors. Ma [10] investigated insulation degradation in excitation circuits and found that the accumulation of carbon powder and oil pollution led to a non-linear decline in resistance. These faults typically manifested as unstable with weak leakage currents, creating detection blind spots for conventional fixed-threshold criteria. Similarly, the authors in [11] and [12] identified “unstable” grounding phenomena in large hydrogenerators, where fault points only made contact under specific centrifugal forces. Huang, Chen, Zhao, and Wang [13] further emphasized that failure to detect such covert faults early could lead to catastrophic consequences,

Manuscript received 7 October, 2025; accepted 27 December, 2025.
This research was supported by the Technical Development Project “Software Design of Scanning Frame Controller” commissioned by Harbin Huamei Power Station Auxiliary Equipment Co., Ltd. under Grant No. HKJ-HX2025-18.

such as conducting rod fractures. These findings collectively suggest that the detection algorithms must be robust enough to capture transient and weak fault signatures.

To overcome the limitations of passive monitoring, active methods such as "Ping-Pong" switching or low-frequency injection have been widely adopted in the industry. Although the authors in [14]–[16] validated the theoretical accuracy of these injection methods in steady-state conditions, recent engineering reports have exposed severe limitations. The field analyses by the authors in [17] and [18] revealed a critical hazard: bridge resistors of external DC insulation monitoring devices that are often coupled into the injection protection sampling circuit. This alteration of the circuit topology distorted the injected signal, leading to maloperation or misjudgment. Furthermore, the response speed of these active methods is inherently limited by the injection period, making them less effective for the rapid dynamic faults mentioned earlier.

Compared to hardware conflicts, the rotor-to-ground capacitance poses a more fundamental threat to passive protection schemes based on harmonic analysis, particularly in units with complex cooling structures. Li [19] explicitly states that for dual water-cooled generators, the massive distributed rotor capacitance significantly affects the voltage establishment process during switching sampling. Martín, Guerrero, Mourelo, and Platero [20] suggest avoiding the transient process associated with the charging/discharging of the equivalent rotor winding-to-ground capacitance, which can significantly slow down the protection response speed. Tan [21] also reported that sudden voltage changes damped oscillations in the rotor circuit due to capacitive effects, directly interfering with signal extraction.

Crucially, existing methods often treat capacitance merely as a noise source. Ji [22] suggests that to prevent false alarms caused by capacitance fluctuations, common practice is to reduce protection sensitivity. However, this approach introduces a core conflict: even with relatively small capacitance, its coupling effect significantly alters the fault voltage characteristics. Existing models indicate that this non-linear coupling inevitably leads to misjudgment or refusal to operate.

As illustrated in Table I, although current methodologies offer solutions to specific engineering problems, a mathematical framework capable of quantifying the influence of rotor capacitance on fault harmonic characteristics remains absent. To bridge this gap, this paper establishes a full-parameter model. Utilizing the proposed amplitude deviation factor for error analysis, we systematically reveal the non-linear mechanism by which C_g affects harmonic voltage amplitudes during DC- and AC-side faults, grounded in the classical equivalent circuit of the excitation system. Significantly, this work identifies detection blind spots resulting from the oversight of capacitive effects in existing studies, particularly under adverse operating scenarios.

TABLE I. COMPARISON OF EXISTING ROTOR GROUND FAULT DETECTION METHODS AND RESEARCH GAPS.

Method Category	Key Focus/Advantages	Limitations & Research Gaps
Fault Mechanism Analysis	Investigated failure causes in large units (e.g., carbon accumulation, dynamic contact).	Focuses on physical maintenance or offline analysis; Lacks online electrical detection algorithms for dynamic faults.
Active Injection Schemes	Independent of operating states; High accuracy in steady states.	Severe hardware conflicts with external devices (e.g., DC monitors); Slow response speed limited by injection cycles.
Traditional Strategies for Capacitance	Acknowledged the interference of rotor capacitance in large-scale units.	Passive handling: Relies on time delays or reducing sensitivity (Desensitization) to avoid maloperation; Lacks a quantitative model to correct errors.
Proposed Method	Full-parameter modeling & Error quantification.	The non-linear coupling between simulated C_g and high-impedance faults is clarified; a blind area identification method based on the amplitude deviation factor is proposed

III. MECHANISM OF HARMONIC AMPLITUDE DEVIATION INDUCED BY ROTOR CAPACITANCE

The system under study is a static excitation system for a synchronous generator, employing a six-pulse thyristor rectifier. The neutral point is grounded via a detection resistor [23], [24]. A simplified schematic of the rotor ground fault detection system is presented in Fig. 1.

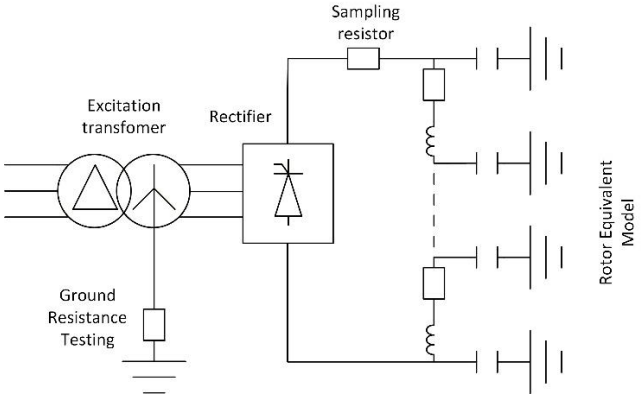

Fig. 1. Simplified schematic diagram of the ground fault protection system.

Figure 1 depicts the excitation system, with the rotor represented by a multi-segment series R-L model with node-to-ground capacitance. Since the parasitic ground capacitance of the excitation transformer is much less than the rotor ground capacitance of large-scale units (0.5 μF–3 μF), its shunting effect is ignored [4].

Table II lists the detailed design parameters of the generator and the main parameters measured on site, which are used for mathematical analysis and simulation.

TABLE II. DETAILED DESIGN PARAMETERS OF THE GENERATOR.

Parameter	Value
Rated Capacity	412 MVA
Rated Power	350 MW
Rated Stator Voltage	21 kV
Rated Stator Current	11320.59 A
Rated Frequency	60 Hz
Rated Excitation Voltage	622.39 V
Rated Excitation Current	1555.24 A
Stator Winding DC Resistance (per phase)	0.001 Ω
Rotor Winding DC Resistance	0.3388 Ω
Rotor Coil Self-inductance	2.2155 H

Given the focus on DC and low-frequency signals,

traveling wave effects are negligible, since the wavelengths exceed the physical dimensions of the rotor. C_g is simplified to a lumped parameter connected between the rotor and the ground.

To reduce the complexity of the problem to a first-order system, this study employs a minimally sufficient equivalent linear model, as illustrated in Fig. 2.

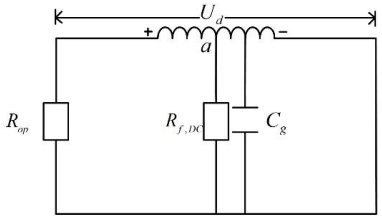

Fig. 2. Rotor equivalent circuit diagram.

The excitation system and the rotor-side network can be represented as follows.

– The excitation voltage is modeled as a DC voltage source.

– The rotor branch comprises the fault resistance ($R_{f,DC}$) and C_g.

– A sampling resistor (R_{op}) is connected in series between the voltage source and the rotor branch.

– All components are assumed to be linear, and temperature effects are ignored.

The excitation circuit follows the dynamics of a classical first-order RC response [25], where the system time constant is governed by the fault resistance and the capacitance to the ground

$$\tau = \left(R_{\text{op}} \parallel R_{f,DC}\right) C_g = \frac{R_{\text{op}} R_f}{R_{\text{op}} + R_f} C_g. \tag{1}$$

Under the influence of the rectified voltage, the transient response of the detection resistor voltage is governed by

$$v_{op}(t) = v_{op}\left(1 - e^{-t/\tau}\right). \tag{2}$$

In large-scale generator sets, a substantial increase in C_g directly extends the duration of the transient response. Let t_s denote the settling time for the system to achieve a steady state. Then, the relationship is given by

$$t_s\left(C_g\right) = -R_{\text{eq}} C_g \ln \varepsilon, \tag{3}$$

where $R_{\text{eq}} = \dfrac{(R_f R_{\text{op}})}{(R_f + R_{\text{op}})}$ represents the equivalent parallel resistance.

Figure 3 illustrates the dependence of the system's transient settling time (t_s) on the rotor ground capacitance. The solid curve represents the precise theoretical settling time derived from (3), while the dashed line depicts the conventional engineering approximation of 3τ.

It is evident that as C_g increases from 0.1 μF to 3.5 μF, the settling time extends linearly, reaching nearly 80 ms. This duration reveals a fundamental conflict with the data acquisition logic of the main digital protection relays. Standard digital algorithms typically employ a full-cycle discrete Fourier transform (DFT) to extract harmonic components, utilizing a data window of only one fundamental cycle (i.e., 20 ms at 50 Hz) to ensure fast fault clearance [26].

Since the physical charging process (approximately 80 ms) significantly exceeds this algorithmic observation window (20 ms), traditional protection logic inevitably performs calculations on the transient rising edge rather than on the steady-state signal. Consequently, directly using these transient sampled values to calculate the fault resistance R_f results in a significant negative deviation, causing the protection system to underestimate the insulation resistance.

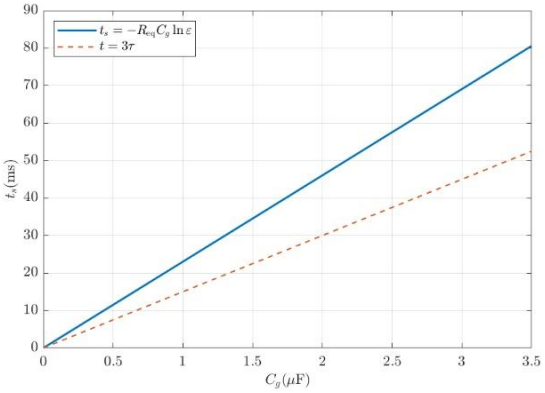

Fig. 3. Settling time required for the response of the system under varying ground capacitances.

Before investigating non-linear errors induced by C_g, it is essential to first establish an ideal model that neglects capacitive effects [27].

From a common-mode perspective, the excitation system can be simplified into the equivalent model shown in Fig. 4. When a ground fault occurs, the fault current flows through the fault resistance and the corresponding phase winding, closing the loop via the sampling resistor.

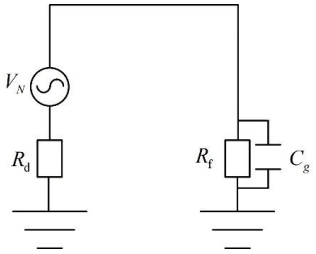

Fig. 4. Equivalent circuit diagram from the common-mode perspective.

The voltage across the detection resistor can be derived from the common-node equivalent circuit [28] as

$$V_g^{\text{acfault}}(t) = I_f(t) R_g = \frac{R_g}{R_f + R_g} V_m \sin(\omega t). \tag{4}$$

Equation (4) reveals that the signal measured under AC fault conditions consists mainly of the fundamental frequency, a characteristic also verified in static excitation systems [29]. Therefore, disregarding negligible higher-order harmonics, the spectrum is represented as

$$\mathcal{F}\{V_g^{\text{ac}}\}(f) \approx K_{\text{ac}} \delta(f - f_1). \tag{5}$$

A ground fault that occurs on the rectified DC side fundamentally distorts the inherent conduction sequence of

the thyristor bridge and redistributes the branch currents. This phenomenon disrupts the balanced operation of the six-pulse rectifier, leading to pronounced voltage ripples at the output terminals. From a common-mode point of view, the neutral point potential of the excitation system is no longer anchored; instead, it exhibits a complex temporal profile comprising a base DC component with multiple superimposed AC harmonics.

Under ideal operating conditions, the spectral content of a three-phase bridge rectifier is predominantly characterized by the DC average value and characteristic harmonics of the order of 3 k (k = 1, 2, …), which arise from periodic switching of power electronic devices. However, the introduction of a DC-side ground fault breaks the circuit symmetry, inducing a shift in the neutral point potential. This asymmetry triggers the emergence of non-characteristic harmonics, most notably the third-order harmonic, in the common-mode voltage spectrum. In systems where the capacitive coupling to ground is assumed to be negligible, the neutral point voltage is approximated as

$$V_g^{\text{dcfault}}(t) \approx \frac{R_g}{R_f + R_g} V_{dc}(t) = \\ = \frac{R_g}{R_f + R_g}\left[V_{dc0} + \sum_{m=1}^{\infty} V_m^{\text{ripple}} \cos(3m\omega t)\right]. \quad (6)$$

Consequently, the spectrum of V_{gdc} is inherently characterized by third-order harmonics

$$S_{dc}(f) = \mathcal{F}\left\{V_g^{dc}\right\} = \\ = \frac{R_g V_{dc0}}{R_f + R_g}\delta(f) + \frac{R_g}{R_f + R_g}\sum_{m\geq 1}\frac{V_m^{\text{ripple}}}{2}\Phi_m(f). \quad (7)$$

As illustrated in Fig. 5(a), when a ground fault occurs on the AC side, the voltage spectrum is dominated by the fundamental component (n = 1), while higher-order harmonics are negligible. Figure 5(b) reveals that during a DC-side ground fault, the fundamental component is suppressed and the spectrum is characterized by a significant third harmonic component (n = 3). In the presence of C_g, the equivalent frequency-domain admittance of the rotor fault based on the aforementioned model is altered. The frequency response function of the neutral point voltage can be expressed as [27]

$$H_g\left(j\omega; C_g\right) = -\frac{\frac{1}{R_f} + j\omega C_g}{\frac{1}{R_g} + \frac{1}{R_f} + j\omega C_g}. \quad (8)$$

To quantitatively evaluate the variations in harmonic amplitude induced by the rotor-to-ground capacitance, an amplitude deviation factor (A_g) is defined. This factor represents the ratio between formula (8) and the ideal capacitor-free state

$$A_g(\omega; C_g) = \frac{\left|V_g(j\omega; C_g)\right|}{\left|V_g(j\omega; 0)\right|} = \frac{\left|H_g(j\omega; C_g)\right|}{\left|H_g(j\omega; 0)\right|} = \\ = \frac{\sqrt{\left(\frac{1}{R_f}\right)^2 + (\omega C_g)^2}}{\sqrt{\left(\frac{1}{R_g} + \frac{1}{R_f}\right)^2 + (\omega C_g)^2}} \times \frac{R_g + R_f}{R_g}. \quad (9)$$

The coefficient A_g quantifies the normalized amplitude deviation relative to the ideal non-capacitive baseline, forming the theoretical basis for harmonic analysis. Figures 6 and 7 depict the amplitude response characteristics against varying C_g. For C_g up to 3 μF, the fundamental deviation is negligible, indicating strong AC-fault signal penetration and stable detection coverage. High-frequency harmonics exhibit a rapid surge of amplitude, significantly outpacing the fundamental one. This behavior results from a reduced high-frequency capacitive reactance that induces a bypass effect, forcing the common-mode voltage drop primarily across the detection resistor R_g.

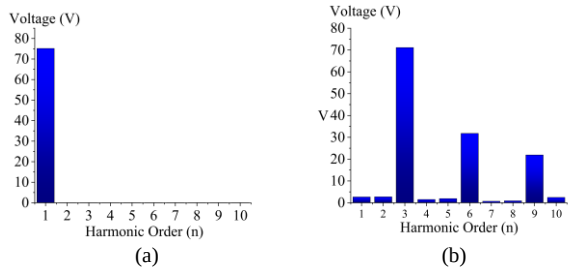

(a) (b)

Fig. 5. Equivalent circuit diagram from the common-mode perspective.

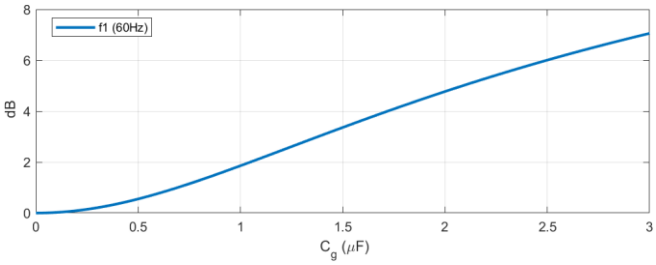

Fig. 6. Change in the amplitude of the fundamental frequency component f_1 under AC-side fault conditions.

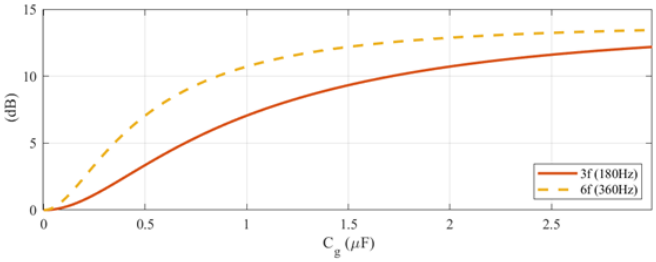

Fig. 7. Amplitude change of the characteristic harmonics $3f_1$ and $6f_1$ under DC-side fault conditions.

As the detection resistor constitutes the sole physical interface that links the excitation system to the ground, its selection of resistance is critical to fault detection sensitivity. In high-resistance grounding systems, fault currents are inherently restricted to extremely low levels (typically < 10 A). Consequently, the resistance of R_g must be sufficiently high to ensure that the current flowing through the detection branch remains negligible compared to the maximum allowed fault current threshold. This is essential to prevent protection

maloperation or excessive total ground fault current induced by the shunt effect of R_g .

According to Fig. 4, based on the worst-case design principle, the strict physical lower bound of the resistance is determined by

$$R_g \geq R_{g,\min}^{\text{safe}} = \frac{V_{\text{n}}}{I_{\text{limit}}}, \tag{10}$$

where $R_{g,\min}^{safe}$ denotes the minimum safe detection resistance required to keep the ground current below the allowable current limit I_{litmit} .

During the incipient stage of rotor insulation degradation, the detection resistor must facilitate a voltage signal of sufficient magnitude to transcend both the quantization errors of the acquisition circuitry and the ambient electromagnetic noise floor. Consequently, by specifying the maximum target fault resistance and the minimum reliable detection threshold, the stringent lower bound of the detection resistance required to maintain adequate sensitivity is determined as follows

$$R_g \geq R_{\text{g,min}}^{\text{safe}} = \frac{V_{\text{th}} R_{\text{f}}}{V_{\text{n}} - V_{\text{th}}}. \tag{11}$$

While the capacitive-coupled noise V_{noise} scales linearly with R_g, the fault signal V_f exhibits diminishing marginal gains due to the non-linear voltage-divider characteristic. Beyond a critical resistance threshold, the incremental noise outweighs the incremental signal gain, leading to deterioration of the signal-to-noise ratio (SNR) and potential hardware channel saturation. By balancing the competing requirements of signal sensitivity and noise immunity, the upper bound recommended for engineering applications is established as $R_{g,max}$ approximately 2000 Ω

$$\Omega_{\text{opt}} = \left\{ R_g \,\middle|\, R_{g,\min}^{\text{safe}} < R_g < R_{g,\max}^{\text{noise}} \right\}. \tag{12}$$

Figure 8 provides a quantitative verification of the resistor selection boundaries by simulating the system response under limiting conditions.

The red curve represents the maximum short-circuit current flowing through the detection branch under the worst-case operating condition, a solid metallic ground fault (R_f = 0 Ω). This curve explicitly verifies the impact of the shunt effect: as R_d decreases, the shunt current increases exponentially. The blue curve illustrates the voltage of the fault signal under high-resistance fault conditions (R_f = 20 KΩ). To accommodate parameter uncertainties, such as fluctuations in rotor capacitance and grid voltage ripples, a sufficient voltage margin is required above the sensitivity limit (dashed blue line, 15 V) [30]. The curve demonstrates that an overly large R_d would attenuate the valid signal, reducing the SNR.

Consequently, the green region (500 Ω–2000 Ω) identifies the feasible engineering interval that simultaneously satisfies the safety constraint under worst-case faults and the sensitivity requirement under parameter uncertainties.

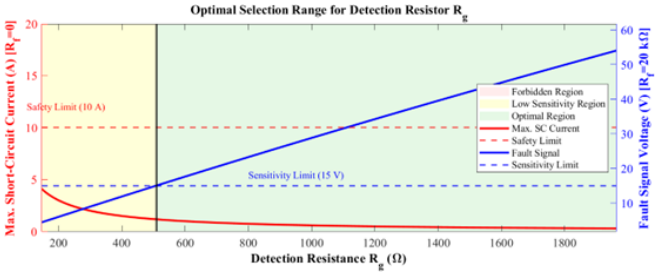

Fig. 8. Amplitude change of the characteristic harmonics $3f_1$ and $6f_1$ under DC-side fault conditions.

IV. Simulation Analysis of the Impact of Ground Capacitance on Detection Blind Spots and Resistance Boundaries

The proposed error analysis method for rotor ground faults was validated through simulations conducted in PSCAD/EMTDC [31], [32]. Figure 9 illustrates the simplified schematic of the simulation model, which represents a large-scale synchronous generator and its associated excitation system. In this model, the excitation rectifiers are controlled with a firing angle set to 54.0 °, and the pulses are enabled by a logic constant set to "True" to ensure stable operation. To accurately simulate fault characteristics along the winding, the rotor winding is modeled as a distributed parameter model consisting of four uniform sections. The detailed parameters of the simulated system are listed in Table I.

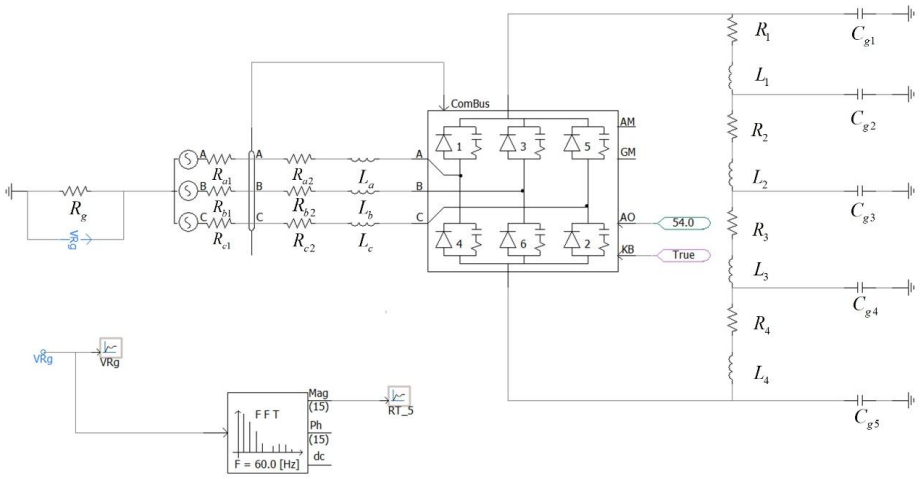

Fig. 9. Simulation model.

Following the theoretical analysis in Section III, the simulation parameters are specifically selected to reflect the capacitance characteristics of large-scale units. For large-scale generating units, particularly those employing water cooling systems, the extensive surface area of the rotor windings and the high permittivity of the cooling medium result in significant parasitic capacitance. Field experiences and protection guidelines [4], [9] indicate that rotor ground capacitance typically ranges from 0.5 μF to 2 μF, and can exceed 3 μF when including surge absorption capacitors and cabling. Therefore, this study sets the simulation range from 0.1 μF (baseline) to 3 μF (worst-case scenario) to comprehensively cover the potential operating conditions of large-scale units.

To evaluate the detection capacity of the system under high-capacitance operating conditions, this study selects a representative range of fault resistance values to comparatively analyze the voltage response in fault states against the fault-free background noise. Simulation experiments are conducted assuming that the ground fault occurs at the positive pole of the rotor winding. As illustrated in Fig. 10, fault-free background noise is observed to surge from 13.36 V to 166.68 V due to increased C_g. This trend is consistent with the impedance characteristics derived from the equivalent circuit model in Fig. 4. Considering the excitation harmonic voltage as a common-mode source (V_n), the steady-state background voltage ($U_{background}$) across the detection resistor can be formulated as follows

$$U_{background} \approx V_n \times \frac{R_d}{\sqrt{R_d^2 + X_{c_g}^2}}. \tag{13}$$

Equation (13) indicates that as C_g increases, the capacitive reactance term ($1/\omega C_g$) diminishes, thereby increasing the voltage divider ratio.

Under normal operating conditions, the resistance to rotor insulation is ideally infinite ($R_f \to \infty$). In this state, the sampling voltage is determined solely by C_g, forming the "healthy baseline" ($U_{baseline}$)

$$Z_g = \frac{R_f \times X_c}{R_f + X_c}. \tag{14}$$

As the fault resistance R_f increases toward infinity, the limit of the impedance is

$$\lim_{R_f \to \infty} Z_g = X_c. \tag{15}$$

This implies that as the fault resistance increases, the resistive branch gradually becomes an open circuit, and the system's impedance characteristics revert to the pure capacitive state. Consequently, the measured voltage must asymptotically approach the $U_{baseline}$.

Figures 10 and 11 reveal that the detection system sensitivity exhibits a significant dependence on the rotor ground capacitance parameter. Under low-capacitance conditions, there is a distinct identification margin between the amplitude of the fault signal and the background noise. However, when C_g exceeds 2 μF, the discrepancy between the two diminishes drastically, causing the curves to converge. This phenomenon introduces a dilemma for protection threshold setting: If the detection threshold is calibrated on the basis of low-capacitance conditions, the amplified background noise resulting from an environment-induced increase in C_g will lead to protection maloperation; if a higher threshold is set on the basis of high-capacitance conditions, high-impedance faults under low-capacitance conditions may be missed, triggering a refusal to operate. Figure 12 shows that the voltage margin between the fault state and the healthy state is merely 0.08 V (approximately 0.05 of the normal value). This minute difference falls entirely within the range of practical engineering measurement errors and grid fluctuations. Consequently, the system enters a state of saturation of sensitivity, where the harmonic amplitude becomes insensitive to variations in fault resistance. This confirms that, for the 350 MW unit investigated in this study, the aforementioned phenomenon occurs once the ground capacitance of the rotor exceeds a specific threshold.

Figure 13 illustrates a significant negative correlation between the fundamental amplitude of the detection voltage and the fault resistance during an AC-side fault.

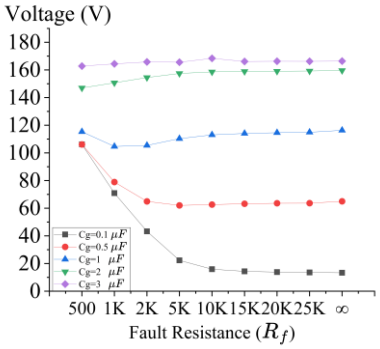

Fig. 10. Amplitude variation characteristics of the third harmonic voltage.

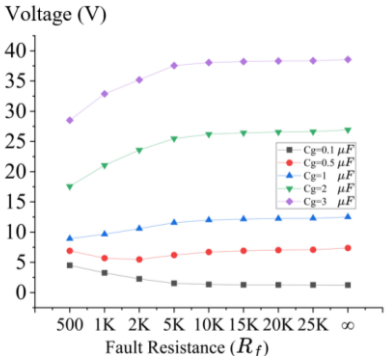

Fig. 11. Amplitude variation characteristics of the fundamental voltage during DC-side faults.

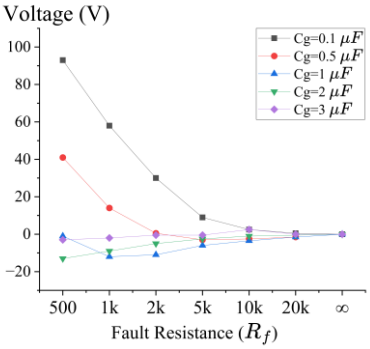

Fig. 12. Differentiation margin between fault signals and background noise.

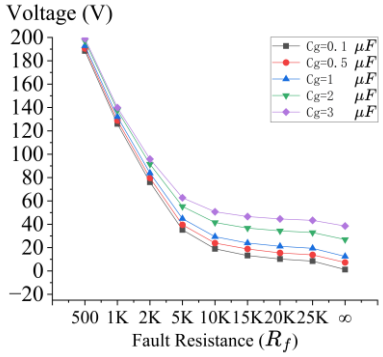

Fig. 13. Amplitude variation characteristics of the fundamental voltage during AC-side faults.

Regardless of the variations in the rotor-to-ground capacitance and fault resistance, this monotonic decrease phenomenon remains consistent. As the fault resistance increases, the detection voltage trends downward, with the steepest decline observed in the low-resistance region (e.g., < 5 kΩ). Under the same fault resistance, although an increase in capacitance slightly elevates the voltage amplitude, the discrepancies between curves of different capacitances are negligible. This indicates that capacitance is not a dominant factor affecting the fundamental amplitude under AC fault conditions, and thus does not significantly interfere with the sensitivity of fundamental-based fault detection.

To rigorously quantify the shift in detection boundaries, Fig. 14 selects two representative fault scenarios for each capacitance level: the minimum fault resistance (R_f = 500 Ω) and the "Critical Crossover Resistance" (defined as the threshold resistance where the parasitic 3rd harmonic amplitude begins to exceed the fundamental component). As illustrated in Fig. 14, the impact of capacitance on this misjudgment boundary is quantified through three distinct phases:

– when C_g = 1 μF (Figs. 14(a) and 14(b)), the phenomenon in which the third harmonic amplitude exceeds the fundamental amplitude occurs only in the high-resistance region where R_f reaches 20 kΩ;

– when it increases to 1 μF (Figs. 14(c) and 14(d)), the critical fault resistance for this phenomenon decreases to 2 kΩ;

– when C_g further increases to 3 μF (Figs. 14(e) and 14(f)), the critical fault resistance is further reduced to 1 kΩ.

The comparative analysis in Fig. 14 reveals a precipitous decline in this critical resistance threshold as the rotor capacitance expands. The fundamental physical driver for this trend lies in the frequency-dependent impedance characteristic of the rotor capacitance. As capacitance increases, its reactance to high-order harmonics decreases ($X_c \rightarrow 1/f$), effectively creating a bypass path. This characteristic amplifies the third harmonic current, causing it to dominate the spectrum and surpass the fundamental component.

If traditional fixed threshold- or ratio-based criteria are adopted, the protection system will erroneously identify the 3rd harmonic as the dominant component, thereby misclassifying such an AC-side fault as a DC-side fault.

It was investigated the sensitivity of the third harmonic voltage to DC-side fault locations across the entire rotor winding (25 %, 50 %, 75 %, 100 %). Table III summarizes the quantitative results of the third harmonic voltage under varying R_f and C_g.

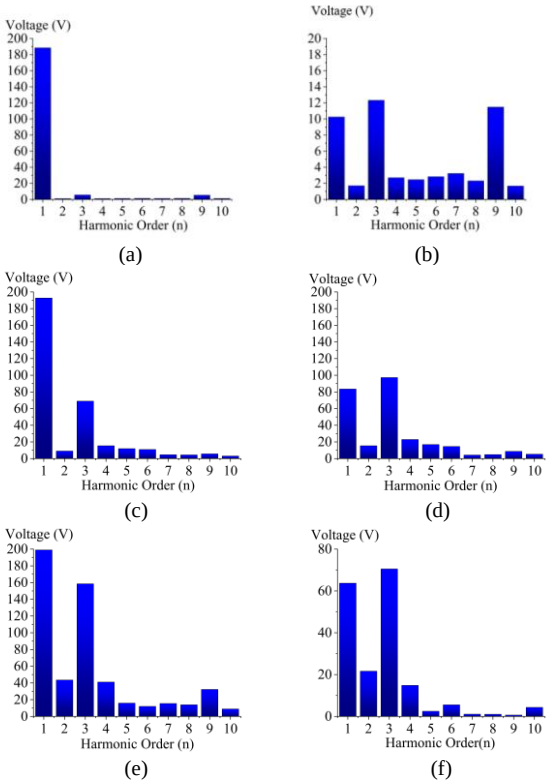

Fig. 14. Harmonic voltage profiles under different conditions: (a) R_f = 500 Ω, C_g = 0.1 μF; (b) R_f = 20 kΩ, C_g = 0.1 μF; (c) R_f = 500 Ω, C_g = 1 μF; (d) R_f = 2 kΩ, C_g = 1 μF; (e) R_f = 500 Ω, C_g = 3 μF; (f) R_f = 1 kΩ, C_g = 3 μF.

As shown in Table III, regardless of fault location, the trend of amplitude variation of the third harmonic voltage remains robust, confirming that the stability of these characteristics originates from the inherent physical structure of the system rather than parameter perturbations.

Meanwhile, under extreme conditions (e.g., grounding impedance > 1 kΩ or capacitive coupling < 5 nF), the signal-to-noise ratio (SNR) of the fault signal deteriorates sharply. Consequently, the third harmonic voltage during faults becomes indistinguishable from baseline values under healthy conditions. This degradation, termed feature submersion, critically compromises the sensitivity of conventional protection criteria and thereby introduces significant protection areas that are blind.

The generator data presented in Table IV correspond to a 5 kVA synchronous generator, which is directly sourced from existing research documented in [33].

Table V details the third harmonic voltage response characteristics of the 5 kVA generator unit under various combinations of fault resistance and rotor-to-ground capacitance. The data reveal that as the rotor-to-ground capacitance C_g increases from 0.1 μF to 3.0 μF, the background noise voltage under healthy insulation conditions surges from 4.61 V to 83.43 V, a significant baseline drift that severely compresses the dynamic detection range; specifically, while a severe ground fault (500 Ω) in a low-capacitance environment (0.1 μF) triggers a distinct voltage shift of approximately 53.9 V, the same fault condition under high-capacitance scenarios (3.0 μF) induces a negligible

variation of less than 1 V, where the fault signature is almost entirely submerged by the elevated background noise, quantitatively confirming that strong capacitive effects force conventional harmonic protection into a region of sensitivity saturation and create an inherent detection blind spot. Figure 15 visually demonstrates the severe distortion of the AC-side ground fault signal under specific high-resistance and strong-capacitance coupling conditions (Fig. 15(a): 5000 Ω 1 μF; Fig. 15(b): 1000 Ω 3 μF).

TABLE III. DISTRIBUTION OF THIRD HARMONIC VOLTAGE ACROSS THE ROTOR WINDING.

Fault at 25 %					
$R_g(\Omega)/C_g(\mu F)$	0.1	0.5	1.0	2.0	3.0
500	74.58	75.10	87.918	99.61	112.68
1K	54.35	61.95	88.69	119.7	132.96
2K	35.60	56.36	95.96	136.08	147.18
5K	19.76	57.13	105.8	149.02	157.60
10K	14.55	58.96	110.51	154.32	161.85
20K	13.42	60.249	113.27	156.92	164.01
Fault at 50 %					
$R_g(\Omega)/C_g(\mu F)$	0.1	0.5	1.0	2.0	3.0
500	69.33	70.22	85.68	101.46	112.50
1K	51.03	60.02	89.1	120.96	132.95
2K	33.83	56.21	97.03	136.67	147.24
5K	19.29	57.49	106.55	149.33	158.26
10K	14.51	59.19	111.01	154.32	162.14
20K	13.52	60.41	113.53	156.99	164.15
Fault at 75 %					
$R_g(\Omega)/C_g(\mu F)$	0.1	0.5	1.0	2.0	3.0
500	69.28	72.43	92.04	114.65	127.29
1K	50.38	62.32	94.49	130.42	143.48
2K	33.32	58.11	100.83	142.59	154.18
5K	19.23	59.06	108.48	152.01	161.41
10K	14.59	59.79	112.11	155.72	163.91
20K	13.67	64.68	114.07	157.68	165.11
Fault at 100 %					
$R_g(\Omega)/C_g(\mu F)$	0.1	0.5	1.0	2.0	3.0
500	74.82	88.09	117.33	153.06	167.15
1K	51.23	73.11	111.95	155.36	166.83
2K	32.86	64.81	108.16	155.95	166.55
5K	19.11	61.8	113.55	158.61	166.75
10K	14.76	64.42	114.71	159.15	166.72
20K	13.72	64.61	115.36	159.46	166.79
∞	13.36	65.00	116.35	159.65	166.38

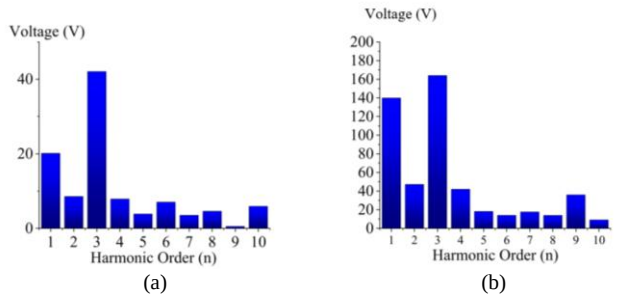

(a) (b)

Fig. 15. Harmonic voltage distribution of a 5 KVA motor under different conditions: (a) R_f = 5000 Ω, C_g = 1 μF; (b) R_f = 1 $k\Omega$, C_g = 03 μF .

Employing authoritative data from the third-party literature for comparative experiments serves to further validate the reliability of the methodology proposed here. The validation results reproduce two key interference phenomena proposed in this paper: First, under DC-side high-impedance grounding and large capacitance conditions, fault features are severely attenuated, inevitably forming detection blind zones. Second, when AC-side faults occur, these adverse conditions excite intense parasitic harmonic components that may exceed the fundamental, exposing the system to a high risk of false positive assessments. This confirms the robustness of the theoretical analysis, demonstrating that such interference mechanisms are inherent characteristics of synchronous generators rather than coincidental artifacts of a specific model.

TABLE IV. PARAMETERS OF THE 5 KVA REFERENCE GENERATOR SOURCED.

Parameter	**Value**
Rated apparent power	5 kVA
Rated voltage (±5 %)	400 V
Frequency	50 HZ
Measured rotor capacitance	157 nF
Rated excitation voltage	22.1 V
Rotor resistance	10 Ω

TABLE V. THIRD HARMONIC VOLTAGE RESPONSE OF THE 5 KVA GENERATOR UNDER FAULT CONDITIONS.

$R_g(\Omega)/C_g(\mu F)$	0.1	0.5	1.0	2.0	3.0
500	53.9	54.09	55.54	62.51	74.24
1k	36.09	38.51	45.12	61.81	73.46
2k	21.78	29.18	42.11	65.05	77.42
5k	10.45	25.71	43.48	68.98	80.78
10k	6.547	25.78	44.86	70.67	82.07
20k	5.05	26.17	45.69	71.64	82.72
∞	4.61	26.79	46.79	72.00	83.43

V. CONCLUSIONS

To address the scientific challenge where the substantial increase in rotor ground capacitance in large-scale synchronous generators renders traditional harmonic detection ineffective, this paper proposes a method for analyzing the error mechanism of capacitive effects and determining detection boundaries based on a full-parameter model.

Based on the “voltage saturation effect” mechanism of the common-mode voltage divider circuit under low capacitive reactance conditions, this method provides an in-depth analysis of the non-linear surge in background noise associated with increasing capacitance. It reveals novel characteristics observed under large-capacitance conditions: the entry of the detection system into a “sensitivity saturation region” and the phenomenon of “spectrum inversion”, where the amplitude of the third harmonic exceeds that of the fundamental wave.

Full-parameter simulation analysis conducted on the PSCAD/EMTDC platform for a large-scale 412 MVA unit indicates that the increase in C_g significantly deteriorates the fault detection environment. Specifically, as C_g increases from 0.1 μF to 3.0 μF, the steady-state background noise surges by more than 12 times, reaching 166.68 V. Under strong capacitance conditions, the amplitude margin between the high-impedance fault signal and the background noise shrinks to merely 0.08 (approximately 5 % of the normal value), forming a physical detection blind zone that cannot be eliminated by algorithms. Furthermore, the capacitance-enhanced high-frequency bypass effect leads to “spectrum inversion” in AC-side faults; consequently, the critical resistance threshold for misjudgment plummets from 20 kΩ to 1 kΩ as C_g increases, making the protection logic highly

susceptible to misclassifying the fault nature. Validated by full winding position scanning, this study confirms the topological consistency of these fault characteristics, thereby revealing that the passive harmonic method suffers from significant detection blind spots under strong capacitance and high-impedance grounding conditions.

The core contribution of this study lies in transcending the conventional qualitative perception of capacitance merely as "noise interference", establishing its quantitative status as "dominant element in the voltage divider network", and quantifying its impact on fault signals via the amplitude deviation factor. We demonstrate that the failure mechanism of the passive harmonic method is not simply signal attenuation, but rather a structural distortion of the system's impedance frequency response characteristics. This finding provides a critical physical reference for the setting of thresholds for existing protection devices. It highlights the necessity of taking into account blind zones of inherent detection formed under severe conditions of strong capacitance and high-impedance grounding, where fault signals become indistinguishable from the healthy baseline. Furthermore, it identifies specific misjudgment intervals induced by the "spectrum inversion" effect during AC-side faults. Consequently, the adoption of multi-criteria fusion algorithms is essential for large-scale unit protection to mitigate the risks of maloperation and refusal to operate associated with reliance on a single passive criterion.

Although this study systematically quantifies the impact mechanism of rotor capacitance on ground fault detection via full-parameter simulations and scaled-model experiments, limitations in experimental conditions necessitate future long-term on-site monitoring data to verify microscopic electric field distribution details. Crucially, under high-capacitance conditions, relying solely on passive signal extraction does not physically eliminate detection blind zones. Merely optimizing the thresholds of existing passive algorithms encounters a theoretical bottleneck, making the introduction of external excitation sources (active detection) an inevitable choice. Given the defined physical applicability limits of passive methods, future work will focus on an "active-passive fusion" strategy. This involves developing multi-criteria fusion algorithms to implement adaptive threshold adjustment based on real-time variations in rotor-to-ground capacitance, thereby maximizing the compression of detection blind zones while suppressing capacitive interference.

CONFLICTS OF INTEREST

The authors declare that they have no conflicts of interest.

REFERENCES

[1] B. Lv, "Analysis and treatment of rotor one point ground fault of generator in hydropower station", *Electric Engineering*, no. 8, pp. 47–49, 2020. DOI: 10.19768/j.cnki.dgjs.2020.08.018.

[2] Y. Li and Y. Liu, "Analysis and handling of rotor one-point grounding accident of thermal power generator", *Mechanical and Electrical Information*, no. 8, pp. 39–40, 2020. DOI: 10.19514/j.cnki.cn32-1628/tm.2020.08.022.

[3] L. J. Powell, "The impact of system grounding practices on generator fault damage", *IEEE Transactions on Industry Applications*, vol. 34, no. 5, pp. 923–927, 1998. DOI: 10.1109/28.720430.

[4] *IEEE Guide for AC Generator Protection*, IEEE Standard C37, 2023.

[5] P. Liu, "Adaptive relay protection identification technology for high-resistance grounding faults in power plant auxiliary power systems", *Standard Technology*, vol. 44, no. 08, pp. 60–62, 2026.

[6] J. Huang and J. Wang, "Analysis and solution of a misoperation event of generator rotor grounding protection", *Henan Electric Power*, pp. 109–111, 2020. DOI: 10.19755/j.cnki.hnep.2020.s1.033.

[7] A. Belan, Z. Eleschova, and F. Janicek, "The cause of false operating of the rotor ground fault protection based on the AC injection method", in *Proc. of 2005 IEEE Russia Power Tech*, 2005, pp. 1–7. DOI: 10.1109/PTC.2005.4524422.

[8] L. Sun, "Analysis of causes of generator protection maloperation in a hydropower station and solutions", *Water Resources & Hydropower of Northeast China*, vol. 42, no. 7, pp. 6–8, 72, 2024. DOI: 10.14124/j.cnki.dbslsd22-1097.2024.07.003.

[9] F. R. Blanquez, M. Aranda, E. Rebollo, and C. A. Platero, "Influence of rotor capacitance in on-line rotor ground fault location method for synchronous machines with static excitation", in *Proc. of 2013 13th International Conference on Environment and Electrical Engineering (EEEIC)*, 2013, pp. 244–249. DOI: 10.1109/EEEIC-2.2013.6737916.

[10] M. Ma, "Analysis and treatment of excitation circuit insulation reduction and high collector ring temperature of generator", *Electric Engineering*, no. S1, pp. 79–81, 2025. DOI: 10.19768/j.cnki.dgjs.2025.25.027.

[11] S. Zhu, "Cause analysis and treatment of rotor dynamic one-point grounding fault of hydro-generator", *Mechanical & Electrical Technique of Hydropower Station*, vol. 48, no. 8, pp. 131–133, 2025. DOI: 10.13599/j.cnki.11-5130.2025.08.032.

[12] X. Zhang, W. Qu, Z. Zhang, and Q. Shu, "Search method for unstable one-point grounding fault of large hydro-generator rotor", in *Proc. of Annual Conference of Automation Committee of China Society for Hydropower Engineering*, 2023, pp. 63–66. DOI: 10.26914/c.cnkihy.2023.010797.

[13] J. Huang, X. Chen, Y. Zhao, and Z. Wang, "Positioning and analysis of rotor short circuit grounding fault of 1000MW brushless excitation turbine generator", in *Proc. of Excellent Papers of Zhejiang Electric Power Society 2024*, 2025, pp. 251–258. DOI: 10.26914/c.cnkihy.2025.053065.

[14] M. Xu and W. Du, "Reliability analysis and suggestions based on generator rotor grounding protection", *Shanghai Energy Conservation*, no. 8, pp. 1346–1351, 2024. DOI: 10.13770/j.cnki.issn2095-705x.2024.08.015.

[15] J. Lv and J. Fu, "Analysis on application and calibration method of three main protections of Jinxin chemical 25MW generator", in *Proc. of the 9th National Petroleum and Chemical Electrical Technology Conference*, 2025, pp. 542–546. DOI: 10.26914/c.cnkihy.2025.004575.

[16] J. Qiao, X. Yin, Y. Wang, Q. Lu, L. Tan, and L. Zhu, "A rotor ground fault protection method based on injection principle for variable speed pumped storage generator-motor", *IEEE Transactions on Power Delivery*, vol. 38, no. 2, pp. 1159–1168, 2023. DOI: 10.1109/TPWRD.2022.3209971.

[17] Z. Yang, L. Wang, and J. Feng, "Process analysis and improvement of bridge resistance of microcomputer DC insulation monitoring device connected into generator injection rotor grounding protection device", in *Proc. of Technical Supervision Professional Technology Exchange Seminar of Electric Power Industry 2024*, 2024, pp. 718–725. DOI: 10.26914/c.cnkihy.2024.050562.

[18] Z. Wang and X. Bi, "Analysis of the cause of rotor grounding protection action tripping", *Mechanical & Electrical Technique of Hydropower Station*, vol. 46, no. 9, pp. 33–35, 2023. DOI: 10.13599/j.cnki.11-5130.2023.09.010.

[19] X. Li, "Analysis of grounding protection design and commissioning of double water internal cooling generator rotor", *Electronic Technology*, vol. 53, no. 12, pp. 328–329, 2024.

[20] C. M. Martín, J. M. Guerrero, P. G. Mourelo, and C. A. Platero, "Ground faults location in poles of synchronous machines through frequency response analysis", *IEEE Transactions on Industry Applications*, vol. 58, no. 1, pp. 113–122, 2022. DOI: 10.1109/TIA.2021.3122412.

[21] G. Tan, "Diagnosis and protection optimization of rotor grounding fault in excitation system of hydro-generator", *Home Appliance Maintenance*, no. 10, pp. 104–106, 2025.

[22] B. Ji, "Cause analysis and preventive measures of abnormal action of generator rotor grounding protection", *Electronic Components and Information Technology*, vol. 9, no. 5, pp. 16–18, 2025. DOI: 10.19772/j.cnki.2096-4455.2025.05.005.

[23] H. Zhilong, "Research and application of one point grounding fast diagnosis method for generator excitation system", in *Proc. of 2021 IEEE Sustainable Power and Energy Conference (iSPEC)*, 2021, pp.

3159–3164. DOI: 10.1109/iSPEC53008.2021.9736107.
[24] X. Chen, L. Xiong, R. Zhou, and Q. Zhang, "Modeling and analysis of generator rotor grounding protection based on combined principle", *Power System Protection and Control*, vol. 41, no. 5, pp. 97–102, 2013.
[25] M. Qi, J. Xia, J. Yu, L. Kang, T. Hou, and H. Su, "Calculation and analysis of DC side output voltage of dual three-phase rectified DC generator considering parasitic parameters of filter capacitor", *Energy and Power Journals*, vol. 46, no. 5, pp. 2092–2103, 2026. DOI: 10.13334/j.0258-8013.pcsee.242419.
[26] H. Xu, H. Zheng, and X. Weng, "Development of a non-contact motor dynamic performance parameter testing and analysis system", *Mechanical and Electrical Information*, no. 12, pp. 14–17, 2024. DOI: 10.19514/j.cnki.cn32-1628/tm.2024.12.004.
[27] G. Fortes, E. Gomes, P. Vilkin, L. M. F. Morais, T. Oliveira, and C. Nunes, "Real-time rotor ground fault protection based on the convolution integral for synchronous motors with static excitation", *IEEE Transactions on Industrial Electronics*, vol. 71, no. 4, pp. 4181–4191, 2024. DOI: 10.1109/TIE.2023.3279556.
[28] F. R. Blanquez, M. Aranda, E. Rebollo, F. Blazquez, and C. A. Platero, "New fault-resistance estimation algorithm for rotor-winding ground-fault online location in synchronous machines with static excitation", *IEEE Transactions on Industrial Electronics*, vol. 62, no. 3, pp. 1901–1911, 2015. DOI: 10.1109/TIE.2014.2336612.
[29] F. R. Blanquez, C. A. Platero, E. Rebollo, and F. Blazquez, "Novel rotor ground-fault detection algorithm for synchronous machines with static excitation based on third-harmonic voltage-phasor comparison", *IEEE Transactions on Industrial Electronics*, vol. 63, no. 4, pp. 2548–2558, 2016. DOI: 10.1109/TIE.2015.2497214.
[30] Y. Zhu, "Generator rotor grounding protection improved by anti-interference algorithm", *Mechanical and Electrical Information*, no. 20, pp. 16–17, 2020. DOI: 10.19514/j.cnki.cn32-1628/tm.2020.20.007.
[31] A. Bermejo, C. A. Platero, F. Blázquez, F. Blánquez, and E. Rebollo, "Verification of a synchronous machine model for stator ground fault simulation through measurements in a large generator", in *Proc. of 2014 2nd International Conference on Artificial Intelligence, Modelling and Simulation*, 2014, pp. 240–245. DOI: 10.1109/AIMS.2014.68.
[32] U. Vargas, A. Ramirez, and G. C. Lazaroiu, "PSCAD simulation and experimental validation of a synchronous generator-based wind turbine generator", in *Proc. of 2018 18th International Conference on Harmonics and Quality of Power (ICHQP)*, 2018, pp. 1–6. DOI: 10.1109/ICHQP.2018.8378812.
[33] C. A. P. Gaona, F. Blázquez, P. Frías, and M. Redondo, "A novel rotor ground-fault-detection technique for synchronous machines with static excitation", *IEEE Transactions on Energy Conversion*, vol. 25, no. 4, pp. 965–973, 2010. DOI: 10.1109/TEC.2010.2040739.